Off-Axis Phase-Matched Terahertz Emission from Two-Color Laser-Induced Plasma Filaments

Y. S. You, T. I. Oh, and K. Y. Kim

Off-Axis Phase-Matched Terahertz Emission from Two-Color Laser-Induced Plasma Filaments

Y. S. You, T. I. Oh, and K. Y. Kim

Institute for Research in Electronics and Applied Physics, University of Maryland, College Park, MD 20742

Abstract

We observe off-axis phase-matched terahertz generation in long air plasma filaments produced by femtosecond two-color laser focusing. Here phase-matching naturally occurs due to off-axis constructive interference between locally generated terahertz waves, and this determines the far-field terahertz radiation profiles and yields. For a filament longer than the characteristic two-color dephasing length, it emits conical terahertz radiation in the off-axis direction, peaked at 4~7° depending on the radiation frequencies. The total terahertz yield continuously increases with the filament length, well beyond the dephasing length. The phase-matching condition observed here provides a simple method for scalable terahertz generation in elongated plasmas.

Corresponding E-mail: kykim@umd.edu

Phase matching is crucial for efficient frequency conversion in many nonlinear processes [1]. So far various phase matching conditions have been studied at a broad range of electromagnetic (EM) frequencies, including infrared, optical, and extreme ultraviolet (EUV) light [1, 2]. At far-infrared or terahertz (THz) frequencies, an EM band which holds promise for numerous imaging and spectroscopic applications [3], there have been several approaches to achieve phase matching conditions [4-6]. In the case of using femtosecond Ti:sapphire lasers operating at 800 nm, zinc telluride (ZnTe) crystals are commonly used to match the group velocity of optical pulses with the phase velocity of THz waves in optical rectification processes [4]. Recently, quasi- and non-collinear phase-matching have been demonstrated in lithium niobate ($LiNbO_3$) crystals with periodical crystal poling [5] and tilted pulse front excitation [6] methods, respectively, where the conventional phase matching scheme described above does not simply apply. In particular, the latter method can produce high energy (hundreds of microjoules) THz radiation, with optical to THz energy conversion efficiency approaching nearly 1% [6]. These schemes, however, are vulnerable to material damage when excited by high-power lasers, which fundamentally limits THz energy scaling.

In contrast, material damage is almost absent in plasma-based THz sources. In particular, femtosecond laser-produced plasma is an ideal medium for scalable THz generation if phase matching can be achieved in plasmas. Previously, Cherenkov-type phase matching was reported in single-color, laser-produced plasmas [7], but the overall conversion efficiency is extremely low because of its relatively poor nonlinear effect in single-color photoionization.

The efficiency can be greatly enhanced by creating plasmas with two-color laser focusing [8-22]. In this scheme, intense THz radiation is produced by focusing an ultrashort pulsed laser's fundamental (ω) and its second harmonic (2ω) pulses in a gas and converting it into a plasma.

Microscopically, the radiation arises from tunneling ionization and subsequent electron current in a symmetry-broken electric field [13-15]. This so-called photocurrent model can explain the microscopic origin of the third order nonlinearity, $\chi^{(3)}$. In this scheme, the resulting THz radiation amplitude is sensitive to the relative phase, θ, between the ω and 2ω pulses in the plasma. Many experiments have shown that the THz amplitude scales as $E_{THz} \propto \sin\theta$ [8-11, 13], assuming constant θ over the entire plasma length (typically <10 mm). However, long plasma filaments ranging from a few centimeters to tens of meters can be formed via femtosecond filamentation in air [23]. In this case, the relative phase θ varies along the filament direction, modulating the amplitude and polarity of local THz waves. Because of this, no THz enhancement was previously predicted in the forward direction [18].

However, in this paper, we report a new type of phase matching condition for efficient THz generation in two-color filamentation. In this scheme, phase matching naturally occurs in the off-axis direction. Figure 1 shows a schematic of THz generation along a long plasma filament. As two-color pulses (ω and 2ω) propagates along the filament, the relative phase changes as $\theta = \omega(n_\omega - n_{2\omega})l / c + \theta_0$, where $n_{\omega,2\omega}$ is the refractive index of plasma filament at ω and 2ω frequency, contributed from both air and plasma dispersion ($n_{filament,\omega} = n_{air,\omega} + n_{plasma,\omega}$), l is the filament length, and θ_0 is the relative phase at the starting point of filament, determined by the frequency doubling process and air dispersion before the plasma filament. Here, $n_{plasma,\omega} \approx \sqrt{1 - \omega_p^2 / \omega^2}$, where ω_p is the plasma frequency (for $n_{air,\omega}$ see [24]). Because of the air-plasma dispersion, the relative phase θ varies over the filament length. Here, the dephasing length, over which the resulting THz polarity remains the same ($0 \leq \theta \leq \pi$), is given by $l_d = (\lambda / 2)(n_\omega - n_{2\omega})^{-1}$, where λ is the wavelength at ω. For example, for pure (no plasma)

atmospheric air, the dephasing length is $l_d \approx 25$ mm at $\lambda = 800$ nm. For a filament with electron density of $N_e \sim 10^{16}$ cm^{-3} [25] in atmospheric air ($\sim 10^{19}$ cm^{-3}), $l_d \approx 22$ mm. Because of this dephasing effect, an oscillatory THz output is expected in the forward direction as the relative phase continuously varies along the filament [18]. This leads to maximal THz generation with filament length $l \approx l_d$.

However, natural phase matching can occur in the off-axis direction. This can be explained by a simple interference effect. For a plasma filament comparable to or longer than the dephasing length, l_d, the THz waves produced along the filament have both positive and negative polarities as shown in Fig. 1. For example, consider the polarity is positive at *Point A* and negative at *Point B* (l_d distance away from *A*). In The waves produced at *Points A* and *B* interfere constructively if the path difference is $\Delta l = P_3 - (P_1 + P_2) = (m + 1/2)\Gamma$, where $m = 0, 1, 2, ...$ and Γ is the THz wavelength. With $m = 0$, the angle for constructive interference is given by $\cos\Theta \approx 1 - \Gamma/(2l_d)$. For $l_d = 20$ mm and $\Gamma = 200$ μm, the emission peaks at $\Theta \sim 6°$. Note that this type of off-axis phase matching is only achieved when the radiation wavelength, Γ, is longer than the source transverse size, D, but shorter than the dephasing length ($D < \Gamma < l_d$). For typical air filamentation, $D < 100$ μm and $l_d \approx 22$ mm, which naturally fulfills the phase matching condition. However, the constraint is not satisfied for conventional optical second harmonic or high harmonic generation (because $\Gamma/D < 0.1$) or THz generation in nonlinear crystals (because $D > \Gamma$ or $\Gamma > l_d$).

To confirm phase-matched THz generation experimentally, a femtosecond laser system capable of delivering 25 fs, 6 mJ pulses at a repetition rate of 1 kHz is used. The laser pulses are focused by a lens, followed by, a 100-μm thick BBO (type-I) crystal which generates second harmonics (see Fig. 1). Both fundamental and second harmonic are focused in ambient air,

creating a plasma filament. THz radiation emitted from the filament is detected by a pyroelectric detector. A silicon filter is used to block unwanted optical and infrared light. Additional filters are used to characterize THz profiles at different frequency bands: a Germanium wafer is used to detect THz frequencies mostly at <10 THz, whereas a 3-mm thick Teflon window is used as a low pass filter to detect <3 THz. For THz imaging, the pyroelectric detector is raster scanned over 5 cm × 3.5 cm, which provides a detection angle of ~10°. THz profiles are measured with two different plasma lengths. In the first set of experiment, the laser energy is limited to ~1.3 mJ with a beam size of 5 mm, and a lens of $f = 15$ cm is used to create a relatively short plasma (~10 mm). The measured far-field THz profiles are shown in Figs. 2(a) and 2(b) at high (Germanium filter) and low (Teflon filter) THz frequencies, respectively. With laser energy of 5 mJ, beam diameter of 10 mm, and lens with $f = 300$ mm, a plasma filament longer than ~40 mm is created. The corresponding THz profiles are shown in Figs. 2(c) and 2(d), at low and high frequency THz frequencies, respectively. Here, the emission angle is ~5° in Fig. 2(c). In the limit where the plasma filament length is much shorter than the dephasing length l_d, all THz waves have the same polarity and constructively interference in the forward direction, producing THz radiation peaked on-axis. Such trend is somewhat shown in Fig. 2(a), obtained with $l \leq l_d$. In this case, the yield, however, is much lower compared to the long filament case in Figs. 2(c)-(d).

We also examine the radiation profiles of THz waves after being focused by a pair of parabolic mirrors. Unlike the conical radiation profiles shown in Fig. 2, the focused THz intensity is peaked on axis with diameter of ~2 mm [19, 20]. This transition is can be explained by Fourier wave propagation or ray-tracing under geometric focusing. The bell-shaped THz profiles are favorable for most practical applications.

We also measure how the total THz yield scales with the plasma length. A lens with $f = 1.5$ m is used to produce ~100 mm long plasma filaments. The resulting THz radiation is collected by a pair of parabolic mirrors and focused into the pyroelectric detector. An iris with aperture diameter of ~2 mm is used to block the THz waves emitted in front the iris, while the THz waves generated behind the iris being unblocked and detected (see the inset in Fig. 4) [12, 18]. Here, THz transmission through the aperture is relatively small and thus ignored. By moving the iris along the filament, we can measure the effective plasma length responsible for the detected THz radiation. The result is shown in Fig. 3. It shows that the THz yield increases with the effective plasma length, regardless of the initial relative phase. Here, we tried three different BBO positions to provide $\theta_0 \approx 0$, $\pi/4$ or $\pi/2$ [13]. Figure 3 shows that the yield continuously increases over the entire scanned length ($l \approx 70$ mm), longer than three times the estimated dephasing length. This suggests we can continuously enhance the THz output by simply increasing the filament length, until the ω and 2ω pulses do not temporally overlap due to plasma dispersion. This gives a theoretical limit of ~4 m. We note that the saturation appeared at ~70 mm is attributed to non-collected THz radiation emitted at the front part of filament due to our limited collection angle.

For a better understanding of THz emission from long plasma filaments, we develop a two-dimensional (2D) THz generation and propagation model. In this model, the local THz source at position r' can be represented by the nonlinear polarization $\tilde{P}$ as

$$\tilde{P}\left(r', \Omega\right) \propto \tilde{A}\left(r', \Omega\right) \sin\left(\theta(z')\right) \exp\left(in_g k_{THz} z' - i\Omega t\right), \tag{1}$$

where $\tilde{A}$ is the local THz amplitude at frequency Ω, given by the microscopic plasma current model [13, 15]. The second term provides a phase-dependent THz amplitude modulation along the filament direction z' owing to the phase mismatch between ω and 2ω pulses. The last term

represents the velocity walk-off between the optical and THz pulse, where n_g is the optical group velocity index of refraction in the filament. The THz far-field is then expressed by integrating the contributions from all local sources over the entire filament plasma volume as

$$E(r,\Omega) \propto \int_V d^3r' \frac{\tilde{P}(r',\Omega)e^{ik_{THz}|r-r'|}}{|r-r'|} \quad . \tag{2}$$

For simplicity, the filament is approximated as a uniform cylindrical plasma with cross section of $\pi a^2 = \pi(D/2)^2$ and length l. At a distance far longer than the filament length ($|r - r'| \gg |r'|$), $\exp(ik_{THz}|r - r'|)/|r - r'| \approx \exp(ik_{THz}(r - r \cdot r'/r))/r$. The integral in the cylindrical coordinate is [26, 27]

$$E(r,\Omega) \propto \tilde{A}(r',\Omega)\frac{\exp(ik_{THz}r - i\Omega t)}{r}\int_0^a d\rho' \int_0^{2\pi} \rho' d\varphi' e^{-ik_{THz}\rho'\cos\varphi\sin\Theta} \tag{3}$$

$$\times \left\{ \left[\int_{-l/2}^{l/2} dz' e^{-ik_{THz}z'(n_g+\frac{\Gamma}{2l_d}-\cos(\Theta))} e^{i\theta_0} \right] - \left[\int_{-l/2}^{l/2} dz' e^{-ik_{THz}z'(n_g-\frac{\Gamma}{2l_d}-\cos(\Theta))} e^{-i\theta_0} \right] \right\} \quad .$$

The far-field THz intensity profile can be approximated as

$$|E(r,\Theta,\Omega)|^2 \propto |\tilde{A}(r',\Omega)|^2 \frac{(\pi a^2)^2 l^2}{r^2}\left(\kappa_1^2 + \kappa_2^2 + 2\kappa_1\kappa_2 \cos(2\theta_0 + \pi)\right)\left(\frac{2J_1(\beta)}{\beta}\right)^2 , \tag{4}$$

where $\kappa_{1,2} = \dfrac{\sin(\alpha_{1,2})}{\alpha_{1,2}}$, $\alpha_{1,2} = \dfrac{k_{THz}l}{2}\left(n_g \pm \dfrac{\Gamma}{2l_d} - \cos(\Theta)\right)$, $\beta = \dfrac{2\pi a}{\lambda}\sin(\Theta)$, and the last term represents circular diffraction. The third term provides a phase-matching condition for efficient THz generation. It depends on two terms α_1 and α_2, instead of one term in most cases, due to the sinusoidal dependence of the local emitters on the phase between the two optical pulses. The condition provides the phase matching angle, Θ_p, for maximal THz generation, given by

$\cos(\Theta_p) = 1 - \dfrac{\lambda}{2l_d}$ for weakly ionized plasma filaments ($n_g \approx 1$). This is the same condition

obtained with the simple interference picture above. Here, Θ_p, is sensitive to the dephasing length and varies with the THz frequency. We note that the THz yield at $\Theta = \Theta_p$ increases with l^2, but total THz yield $\int |E(r,\Theta,\Omega)|^2 \sin\Theta d\Theta$ does not simply increase with l^2 because of the angle-dependent phase-matching term.

Figures 2(e)-(f) show the simulated THz radiation profiles obtained from Eq. (3) under the experimental conditions of Figs. 2(c)-(d). The conical emission for $l \geq l_d$ is well reproduced in Figs. 2(e)-(f) with $\Theta_p \sim 6°$, consistent with the measured peak radiation angle. For $l \leq l_d$, the simulation provides a bell-shaped profile. For instance, Figure 4(a) shows the angular distributions at 1 THz for $l = l_d$, $2l_d$, and $3l_d$. Figure 3(b) shows that Θ_p tends to decrease with increasing THz frequency, consistent with the measured profiles shown in Figs. 2(c)-(d). Figures 4(c) shows the angle-dependent yield $|E(r,\Theta,\Omega)|^2$ at 1 THz as a function of increasing filament length for various angles. At $\Theta \sim 7°$, the yield increases almost with l^2 as predicted in Eq. (3), but it drops after passing the phase-matching angle (see $\Theta = 8°$). We also calculate how the total yield at 1 THz depends on the length of plasma. As shown in Fig. 4(d), when the plasma is shorter than the dephasing length ($l \ll l_d$), the yield is greatly sensitive to the initial phase, consistent with the microscopic behavior [8-11, 13]. However, when the plasma length becomes longer ($l \geq l_d$), the yield increases almost linearly regardless of the initial phase [2]. Here, the constraint $D < \Gamma < l_d$ needs to be satisfied. For example, the total yield at 1 THz with a large source diameter $D = 2$ mm ($\Gamma/D \sim 0.15$) shows only an oscillatory behavior (no overall enhancement) with increasing filament length [see Fig. 4(e)]. With a typical filament diameter ($D \sim 0.1$ mm), the phase matching condition is well satisfied at low THz frequencies [see Fig. 4(f)].

Our model, however, has several limits. It assumes cylindrical, uniform plasma-density filaments and excludes THz absorption and refraction inside the filaments. It also assumes luminal THz phase velocities in free space and linear THz polarization [16, 17]. It also ignores self-phase modulation in air and spectral blue shifts via tunneling ionization occurring over the entire plasma filament. Nonetheless, our simple model well describes the measured THz emission yields and angular profiles, providing a physical insight into macroscopic THz propagation and enhancement processes in plasmas.

In conclusion, we discover off-axis phase-matched THz generation in elongated two-color filamentation. In particular, we find the THz yields and angular distributions are greatly sensitive to the filament and dephasing length. Simultaneously, the yield increases almost linearly with the plasma filament length as a result of off-axis phase matching. Due to this, one can effectively increase THz output by simply extending the plasma filament length with more laser power while keeping the local THz wave strength constant. This method can overcome the saturation effect previously reported [13, 14], mainly caused by overdense plasma creation and laser intensity clamping in filamentation.

References

1. R. W. Boyd, *Nonlinear Optics* (Academic Press, 1992).

2. X. Zhang, A. L. Lytle, T. Popmintchev, X. Zhou, H. C. Kapteyn, M. M. Murnane, and O. Cohen, Nat. Phys. **3**, 270 (2007).

3. D. Mittleman, *Sensing with Terahertz Radiation* (Springer-Verlag, 2002).

4. A. Nahata, A. S. Weling, and T. F. Heinz, Appl. Phys. Lett. **69**, 2321 (1996).

5. Y. S. Lee, T. Meade, V. Perlin, H. Winful, T. B. Norris, and A. Galvanauska, Appl. Phys. Lett. **76**, 2505 (2000).

6. J. A. Fülöp, L. Pálfalvi, S. Klingebiel, G. Almási, F. Krausz, S. Karsch, and J. Hebling, Opt. Lett. **37**, 557 (2012).

7. C. D'Amico, A. Houard, M. Franco, B. Prade, A. Mysyrowicz, A. Couairon, and V. T. Tikhonchuk, Phys. Rev. Lett. **98**, 235002 (2007).

8. D. J. Cook and R. M. Hochstrasser, Opt. Lett. **25**, 1210 (2000).

9. M. Kress, T. Löffler, S. Eden, M. Thomson, and H. G. Roskos, Opt. Lett. **29**, 1120 (2004).

10. T. Bartel, P. Gaal, K. Reimann, M. Woerner, and T. Elsaesser, Opt. Lett. **30**, 2805 (2005).

11. X. Xie, J. Dai, and X.-C. Zhang, Phys. Rev. Lett. **96,** 075005 (2006).

12. H. Zhong, N. Karpowicz, and X.-C. Zhang, Appl. Phys. Lett. **88**, 261103 (2006).

13. K. Kim, J. H. Glownia, A. J. Taylor, and G. Rodriguez, Opt. Express **15**, 4577 (2007).

14. K. Kim, A. J. Taylor, J. H. Glownia, and G. Rodriguez, Nat. Photon. **2**, 605 (2008).

15. K. Kim, Phys. Plasmas **16**, 056706 (2009).

16. J. Dai, N. Karpowicz, and X.-C. Zhang, Phys. Rev. Lett. **103**, 023001 (2009).

17. H. Wen and A. Lindenberg, Phys. Rev. Lett. **103**, 2 (2009).

18. Y. Liu, A. Houard, M. Durand, B. Prade, and A. Mysyrowicz, Opt. Express **17**, 11480 (2009).

19. F. Blanchard, G. Sharma, X. Ropagnol, L. Razzari, R. Morandotti, and T. Ozaki, Opt. Express **17**, 6044 (2009).

20. R. A. Akhmedzhanov, I. E. Ilyakov, V. A. Mironov, E. V. Suvorov, D. A. Fadeev, and B. V. Shishkin, Sov. Phys. JETP **109**, 370 (2009).

21. M. D. Thomson, V. Blank, and H. G. Roskos, Opt. Express **18**, 23173 (2010).

22. I. Babushkin, W. Kuehn, C. Köhler, S. Skupin, L. Bergé, K. Reimann, M. Woerner, J. Herrmann, and T. Elsaesser, Phys. Rev. Lett. **105**, 053903 (2010).

23. A. Couairon and A. Mysyrowicz, *Phys. Rep.*, **441**, 47 (2007).

24. B. Edlén, *Metrologia* **2**, 71 (1966).

25. Y. H. Chen, S. Varma, T. M. Antonsen, and H. M. Milchberg, Phys. Rev. Lett. **105**, 215005 (2010).

26. J. R. Morris and Y. R. Shen, Phys. Rev. A **15**, 1143 (1977).

27. Y. R. Shen, *The Principles of Nonlinear Optics* (Wiley-Interscience, New York, 1984), pp. 110~111.

Figure captions

Fig. 1 (Color online) Schematic of THz emission from a long, two-color laser-produced filament. The phase slippage between 800 nm (red) and 400 nm (blue) pulses along the filament results in a periodic oscillation of microscopic current amplitude and polarity. The resulting far-field THz radiation is determined by interference between the waves emitted from the local sources along the filament.

Fig. 2 Measured far-field THz radiation profiles obtained with (a)(b) 10-mm long and (c)(d) 40-mm long filaments, all obtained by raster scanning of a pyroelectric detector with a silicon filter. Additional Teflon (a-c) and Germanium (b-d) filters are used for low (<3 THz) and high (<10 THz) frequency band transmission. (e)~(f) are simulated THz profiles for the long filament case.

Fig. 3 (Color online) Far-field THz yield as a function of plasma filament length. The inset shows a luminescent image of filament created by two-color laser pulses propagating from left to right. The measurements were done at three different BBO positions, representing three different initial phase differences 0, $\pi/4$, and $\pi/2$.

Fig. 4 (Color online) Simulation results for (a) THz profiles with different plasma length: $l = l_d$, 2 l_d, and $3l_d$ at 1 THz, (b) far-field THz profiles at three different frequencies: 1 THz, 3 THz, and 5 THz, (c) THz yield versus plasma length at various emission angles; $\Theta = 0°$, $3°$, $7°$, and $8°$ at 1 THz, (d) total THz yield versus plasma length with different initial phases $\theta_0 = 0$, $\pi/4$, and $\pi/2$ at 1 THz. Simulated THz yields with increasing plasma length normalized by the dephasing length

for (e) three different filament diameters (0.1 mm, 1 mm, 2 mm) at 1 THz emission and (f) 0.1 mm filament diameter at 1 THz, 10 THz, and 100 THz radiation emission.
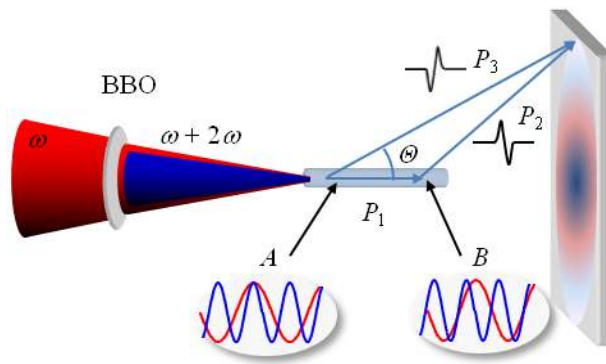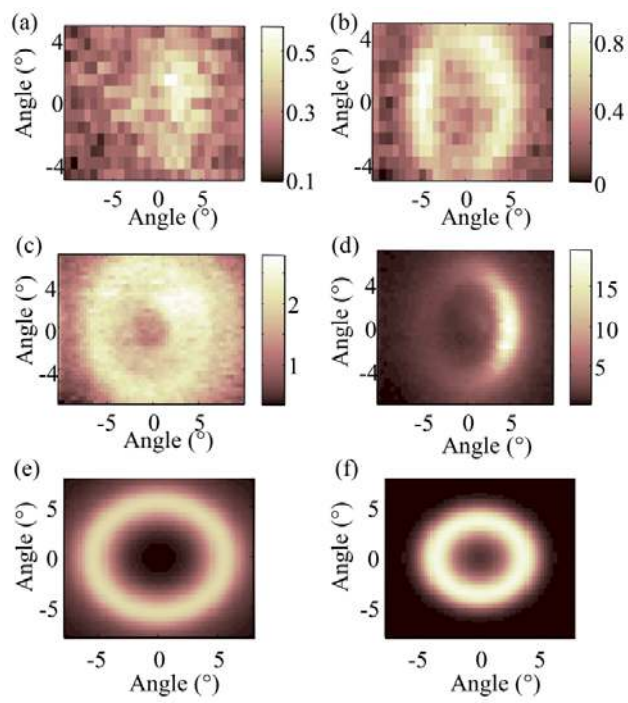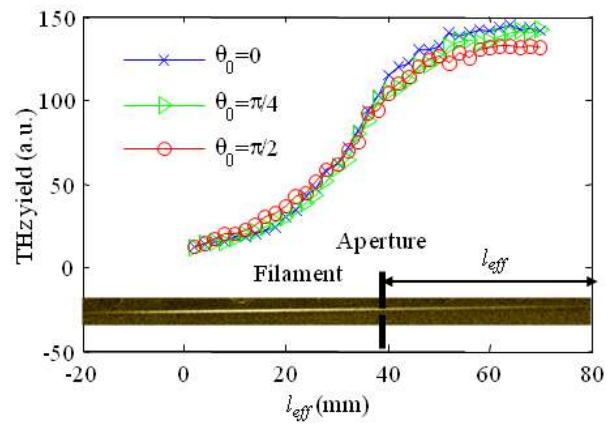
Fig. 1

BBO
ω
$\omega + 2\omega$
P_3
P_2
Θ
P_1
A
B

Fig. 2

Fig. 3

Fig. 4